

Ultra precise determination of $\text{Cs}(nS_{1/2})$ and $\text{Cs}(nD_J)$ quantum defects for sensing and computing: Evaluation of core contributions

Pinrui Shen,¹ Donald Booth,¹ Chang Liu,¹ Scott Beattie,² Claude Marceau,² James P. Shaffer,^{1,*} Mariusz Pawlak,³ and H. R. Sadeghpour^{4,†}

¹*Quantum Valley Ideas Laboratories, 485 Wes Graham Way, Waterloo, Ontario N2L 6R1, Canada*

²*National Research Council Canada, Ottawa, Ontario K1A 0R6, Canada*

³*Faculty of Chemistry, Nicolaus Copernicus University in Toruń, Gagarina 7, 87-100 Toruń, Poland*

⁴*ITAMP, Center for Astrophysics | Harvard & Smithsonian, 60 Garden Street., Cambridge, Massachusetts 02138, USA*

(Dated: December 9, 2024)

We make absolute frequency measurements of Cs Rydberg transitions, $|6S_{1/2}, F = 3\rangle \rightarrow |nS_{1/2} (n = 23-90)\rangle$ and $|nD_{3/2,5/2} (n = 21-90)\rangle$, with an accuracy of less than 72 kHz. The quantum defect parameters for the measured Rydberg series are the most precise obtained to date. The quantum defect series is terminated at δ_4 , showing that prior fits requiring higher order quantum defects reflect uncertainties in the observations. The precision of the measured quantum defects allow for the calculation of Rydberg electric-dipole transitions and fine-structure intervals extrapolated from high principal quantum numbers, to rival that of sophisticated many-body relativistic calculations carried out at low Rydberg principal quantum numbers. We quantitatively predict the contributions to the quantum defect parameters from core polarization and core penetration of Cs inner shell electrons. A new value for the ionization energy, consistent across the $nS_{1/2}$ and $nD_{3/2,5/2}$ Rydberg series, is reported at $31406.46775148(14) \text{ cm}^{-1}$.

Neutral-atom-based quantum simulators and processors are the leading architectures for high fidelity quantum operations while atoms are being used extensively as sensors because of their stability and uniformity. Rydberg atoms are particularly suitable for quantum simulations and metrology, because their properties can be tuned through state selection and the use of electromagnetic fields. Precise knowledge of atomic structure enables engineering of atomic properties. Similarly for basic research, precise measurements of atomic energy levels provide stringent tests of atomic structure calculations, including quantum defect theories, and are critical for the determination of a number of fundamental constants in physics [1–3]. Cesium atoms have been used for searches of the electric-dipole moment of the electron [4–7], among other fundamental quantities. Rapid developments in quantum measurement technologies, such as optical clocks [8–12], neutral-atom-based quantum computing [13–17] and Rydberg-atom-based electric field sensors [18–20] are adding impetus to accurately determine energy levels as well as derived quantities such as electric field polarizabilities and reduced electric-dipole matrix elements. The aim of this work is to improve the accuracy of Cs atomic energy level measurements for advanced applications in quantum sensing.

We present absolute frequency measurements for the Cs transitions $|6S_{1/2}, F = 3\rangle \rightarrow |nS_{1/2} (n = 23-90)\rangle$ and $|nD_{3/2,5/2} (n = 21-90)\rangle$ with an accuracy of $< 72 \text{ kHz}$. By fitting the absolute-frequency measurements to the modified Ritz formula, we determine the most accurate quantum defect parameters of the $nS_{1/2}$, $nD_{3/2}$, and $nD_{5/2}$ series to date, and obtain a new ionization energy, $31406.46775148(14) \text{ cm}^{-1}$. Because of the accuracy

of the underlying term energies, the highest order fitted quantum defect is δ_4 , illustrating that the higher terms, often found in the literature, reflect uncertainties in the measurements. We extract the fine-structure intervals for the nD_J series. The precision of our calculations of electric-dipole transition matrix elements is comparable with that of sophisticated many-body relativistic calculations [21] at low n , where measurements were not carried-out. We calculate the contributions to the quantum defect parameters from core polarization and core penetration. Both effects are found to be in agreement with high level atomic structure calculations.

The experimental cycle begins by collecting Cs atoms in a magneto-optical trap (MOT). The MOT atoms are cooled to $< 10 \mu\text{K}$ using polarization gradient cooling [22, 23]. After the cooling stage, the atoms are optically pumped to the $|6S_{1/2}, F = 3\rangle$ ground state. Subsequently, the trapping magnetic field and lasers are switched off to create a field-free environment for the atoms. During the entire interrogation period, the residual magnetic field is reduced to $< 2 \text{ mG}$ and the stray electric field is reduced to $< 1 \text{ mV/cm}$, using external field compensation [24].

A two-step laser excitation at $\sim 852 \text{ nm}$ and $\sim 509 \text{ nm}$ creates cold Cs Rydberg atoms. The lasers are both locked to a frequency comb that is stabilized to a GPS steered rubidium clock, resulting in laser linewidths of less than 200 Hz and a fractional frequency stability of 1.2×10^{-12} for a 10 s averaging time. The $\sim 852 \text{ nm}$ laser is red-detuned 90 MHz from the $|6P_{3/2}, F' = 2\rangle$ excited state. The $\sim 509 \text{ nm}$ laser is 90 MHz blue-detuned from the resonance between the $|6P_{3/2}, F' = 2\rangle$ state and the target nD_J or $nS_{1/2}$ Rydberg state. The two

lasers are crossed in a perpendicular configuration, both with parallel linear, vertical polarizations. The Gaussian beam waists for the first- and second-step lasers are $w_0 = 3$ mm and $w_0 = 400$ μm , respectively. The lasers are pulsed to excite the Rydberg atoms. The duration of the excitation laser pulses is 30 μs . The pulses overlap in time.

Following the laser excitation pulses, a 2 μs high voltage square pulse is applied to field ionization plates to ionize the Rydberg atoms and project the ions onto a multi-channel plate (MCP) detector. The average number of detected ions generated per laser shot is minimized to < 2 to reduce Coulomb repulsion. The ion pulses are recorded on a multichannel analyzer.

To obtain the Rydberg state spectrum, the frequency of the ~ 852 nm laser is fixed and the frequency of the ~ 509 nm laser is scanned. The laser excitation and ion detection sequence is repeated 40 times for each cold atomic cloud. Twenty clouds are used for each ~ 509 nm laser frequency, resulting in 800 excitation-detection cycles per laser frequency step. The spectroscopy measurements are performed for the $nD_{5/2}$ ($n = 21-90$), $nD_{3/2}$ ($n = 21-90$), and $nS_{1/2}$ ($n = 23-90$) series.

For the $nD_{3/2}$ and $nD_{5/2}$ series, the measured spectrum is fit to a hyperfine-structure-weighted multiline Gaussian function [24]. For the $nS_{1/2}$ series spectrum, a single Gaussian function is used since there is only one allowed hyperfine transition, $|6P_{3/2}, F = 2\rangle \rightarrow |nS_{1/2}, F' = 3\rangle$, and the dominant broadening mechanism is Doppler broadening, at the 200 kHz level. The spectral line frequency is the absolute transition frequency between the $|6S_{1/2}, F = 3\rangle$ hyperfine state and the center of gravity of the Rydberg energy level.

The transition frequencies are corrected to account for the AC Stark shifts caused by the lasers. The AC Stark shift induced by the ~ 509 nm laser is no greater than 500 Hz for the $21D_J$ state. The ~ 852 nm laser induces a measured (36.0 ± 4.8) kHz blue shift of the ground state, $|6S_{1/2}, F = 3\rangle$ [24]. The 36.0 kHz shift is subtracted from the transition frequency and the uncertainty, ± 4.8 kHz, is taken as a contribution to the uncertainty of the resonance frequency.

For the $nS_{1/2}$ series, the DC Stark effect induces a Rydberg level frequency shift. The maximum shift is calculated to be < 1.5 kHz for the $90S_{1/2}$ state [40–42]. For the nD_J series, the DC Stark effect predominantly splits the energy levels because different m_J states have different Stark shifts. It is difficult to resolve the peak splitting when the stray electric field is small, < 1 mV/cm. Thus, the DC Stark effect causes asymmetric line broadening of the nD_J states and is treated as a contribution to the uncertainty of the measured transition frequency. Based on the polarizability of the Cs $nD_{5/2}$ states, the maximum broadening is estimated to be < 49 kHz for the $90D_{5/2}$ state [24, 43].

The Zeeman shift of the ground state is minimized us-

ing microwave spectroscopy [24, 44]. The Zeeman shift was measured to be < 14.3 kHz. The sensitivity to the magnetic field is similar across all Rydberg states because they have the same Landé g -factor. The Zeeman shift is treated as another source of uncertainty.

The shot-to-shot variance dominates the statistical uncertainty. Systematic shifts, most probably associated with residual Stark shifts, can be observed in the plot of the residuals, Fig. 1. The sum of the statistical uncertainty and the systematic uncertainty is no greater than 60 kHz [24]. The statistical standard deviation of the residuals of the modified Ritz formula fit is < 72 kHz for all series.

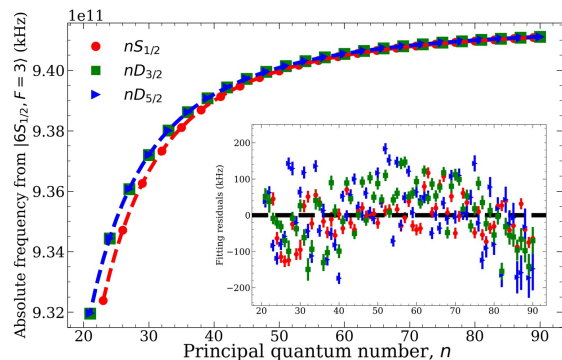


FIG. 1. Absolute frequency measurements for transitions from $|6S_{1/2}, F = 3\rangle$ to the center of gravity of the $nS_{1/2}$, $nD_{3/2}$, $nD_{5/2}$ Rydberg states. Data are presented with a step of $\Delta n = 3$ to avoid crowding. The dashed lines correspond to the modified Ritz formula. The fitting residuals are shown in the inset. The error bars represent the total uncertainty. The statistical variance of the fitting residuals of the $nD_{5/2}$, $nD_{3/2}$, and $nS_{1/2}$ series are 71.2 kHz, 59.1 kHz, and 46.9 kHz, respectively.

The observed term energies of a single Rydberg series can be described by the modified Ritz formula:

$$E_{n,l,J} = E_I - \frac{R}{[n - \delta^{(l,J)}(n)]^2}, \quad (1)$$

where E_I is the ionization energy and R is the reduced mass Rydberg constant, equal to $R_\infty/(1 + m_e/m_{\text{core}})$. Using the current mass of the Cs atom [47], we obtained $R_{133\text{Cs}} = 109736.8627304$ cm^{-1} . The (n, l, J) -dependent quantum defects are

$$\delta^{(l,J)}(n) = \delta_0^{(l,J)} + \sum_{k=1}^{\infty} \frac{\delta_{2k}^{(l,J)}}{[n - \delta_0^{(l,J)}]^{2k}}. \quad (2)$$

We constrain the quantum defects to a three-term expansion, $\delta^{(l,J)}(n) = \delta_0^{(l,J)} + \frac{\delta_2^{(l,J)}}{[n - \delta_0^{(l,J)}]^2} + \frac{\delta_4^{(l,J)}}{[n - \delta_0^{(l,J)}]^4}$, and fit the measured energy levels to Eq. (1), which minimizes the correlations between the ionization energy and the quantum defects present in the fit. The Rydberg state

TABLE I. Quantum defects for the $nD_{5/2}$, $nD_{3/2}$, and $nS_{1/2}$ series obtained by fitting the measured Rydberg energy levels to Eq. (1). The uncertainties are the standard deviations of the fit. For comparison, the quantum defects used in the ARC python calculation package [40] are also listed.

	$nD_{5/2}$ [this work] ($n = 21-90$)	$nD_{5/2}$ [45] ($n = 5-36$)	$nD_{3/2}$ [this work] ($n = 21-90$)	$nD_{3/2}$ [46] ($n = 5, 6, 8-32$)	$nS_{1/2}$ [this work] ($n = 23-90$)	$nS_{1/2}$ [45] ($n = 6-30$)
IE (cm^{-1})	31406.46775168(26)	31406.46767(3)	31406.46775148(28)	31406.4710(7)	31406.46775136(21)	31406.46769(2)
δ_0	2.46631529(14)	2.46631524(63)	2.47545840(13)	2.4754562	4.04935994(17)	4.04935665(38)
δ_2	0.013431(65)	0.013577	0.008339(62)	0.009320	0.238017(18)	0.2377037
δ_4	-0.3613(61)	-0.37457	-0.3769(95)	-0.43498	0.1747(33)	0.255401
δ_6	0.0	-2.1867	0.0	-0.76358	0.0	0.00378
δ_8	0.0	-1.5532	0.0	-18.0061	0.0	0.25486
δ_{10}	0.0	-56.6739	0.0	0.0	0.0	0.0

TABLE II. Numerically computed core polarization contribution, $\delta_{\text{pol}}^{(l,J)}$, and core penetration contribution, $\delta_{\text{pen}}^{(l,J)}$, to the leading quantum defect term of the $nD_{5/2}$, $nD_{3/2}$, and $nS_{1/2}$ series.

series	$\delta_0^{(l,J)}$	$\delta_{\text{pol}}^{(l,J)}$	$\delta_{\text{pen}}^{(l,J)}$
$nD_{5/2}$	2.46631529(14)	1.0482(4)	1.4197(6)
$nD_{3/2}$	2.47545840(13)	1.0625(7)	1.4094(5)
$nS_{1/2}$	4.04935994(17)	0.1320(5)	3.9111(4)

energy is obtained by subtracting the frequency splitting, 5.170855370625 GHz, between the center of gravity of the $6S_{1/2}$ state and the $|6S_{1/2}, F = 3\rangle$ hyperfine state [48] from the measured absolute transition frequencies listed in Table S4 [24], i.e., the energies are referenced to the ground state center of gravity to perform the fitting.

The ionization energies are reported in Table I. The extracted ionization energies for the $nD_{5/2}$, $nD_{3/2}$, and $nS_{1/2}$ states agree within their uncertainties. The uncertainty-weighted average ionization energy is $31406.46775148(14) \text{ cm}^{-1}$. The result agrees with the ionization energy reported in Ref. [45], but is 600 kHz higher than the most recent value presented in Ref. [49], $31406.4677325(14) \text{ cm}^{-1}$. In Ref. [49], Cs samples were prepared in an optical dipole trap that cannot be completely shut-off, leading to a larger AC Stark effect. The ionization energy reported in Ref. [49] was extracted using one Rydberg series, $|nP_J (n = 27-74)\rangle$ where the n step size was 3. In this work, the Cs samples are excited in a field-free environment and the ionization energy is extracted from all of the levels in the three Rydberg series $|nS_{1/2} (n = 23-90)\rangle$ and $|nD_J (n = 21-90)\rangle$. Moreover, the uncertainty of our ionization energy determined by the fit to the modified Ritz formula is further reduced by one order of magnitude.

The non-linear least squares fit to measured energies are shown in Fig. 1 with residues in the inset. The systematic downward trend for the higher principal quantum numbers of the nD_J series is likely caused by DC Stark shifts. The quantum defects for all three series are presented in Table I. Our results show that the $\delta_{2k}^{(l,J)}$ parameters for $k > 2$ for all three series are insignificant within the measurement uncertainties. Several studies

have reported these terms for the same states as non-zero at lower levels of experimental precision [45, 46]. Since the precision of our measurements is two orders of magnitude better than that of the prior work, it is likely that these terms have no physical significance and were fitting parameters that accommodated experimental uncertainties [24].

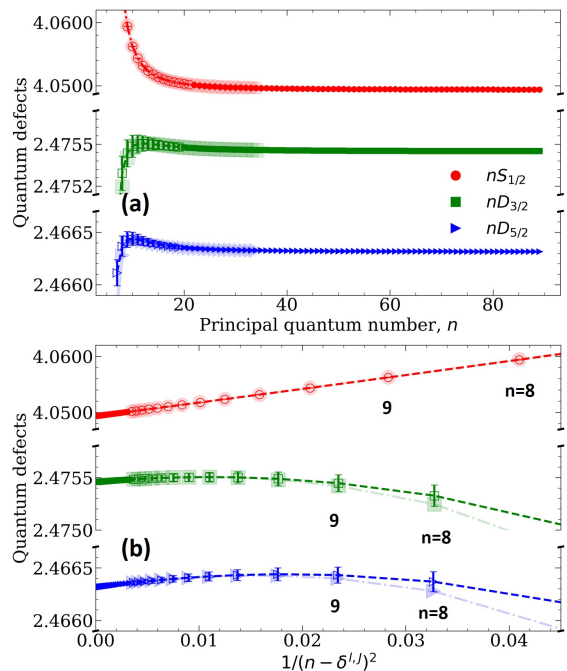


FIG. 2. Experimental quantum defects, $\delta^{(l,J)}$, versus n (a) and $1/[n - \delta^{(l,J)}]^2$ (b), for all measured term series in Cs. Solid markers are the quantum defects measured in this work, while open markers are extrapolated from the experimental measurements. The light color markers represent the values calculated based on previous publications, $nS_{1/2}$ [45], $nD_{3/2}$ [46], and $nD_{5/2}$ [45]. The error bars are acquired by propagating the fitting uncertainty of the quantum defects.

The quantum defect parameters obtained from the measurements in Fig. 2(a) agree well within the uncertainties, even for lower-lying states ($8 < n < 21$), where no measurements were taken. The plots show further evidence that the quantum defect expansion greater than

third order is not required, since our predictions for the $nS_{1/2}$, $nD_{3/2}$, and $nD_{5/2}$ energy levels match the available experimental data at low n . Notably, the trend for both nD_J series is non-monotonic while that of the $nS_{1/2}$ series always decreases as a function of n . The non-monotonic behavior of the nD_J series had been reported in Refs. [45, 46, 50]. The behavior can be viewed more clearly by plotting the quantum defects as a function of $1/[n - \delta^{(l,J)}]^2$, shown as Fig. 2(b). The difference between $nS_{1/2}$ and nD_J is the result of a competition between core polarization and core penetration. Core polarization reduces the quantum defect, more so as the electron effective radius is reduced, i.e., low n . As n increases, the core polarization effect decreases faster than the core penetration effect, which leads to a quantum defect dominated by core penetration.

Weber *et al.* [45] investigated the contribution from core polarization for the nD_J series of Cs and concluded that it is too small to account for the non-monotonic behavior. We quantitatively studied the behavior by numerically calculating the contributions to the quantum defect's leading term from core polarization and core penetration. Using the model potential in Ref. [51] in conjunction with the spin-orbit coupling effect, we calculated the expectation values of the energy due to core polarization and core penetration [24]. The numerically determined contributions to $\delta_0^{(l,J)}$ are presented in Table II. For the nD_J series, the contribution from core polarization is over 40%, much larger than the estimate in Ref. [45], possibly because the second-order dipole polarization corrections were not included [52]. If core polarization is neglected, the nD_J quantum defects become larger as n decreases, similar to $nS_{1/2}$. For the $nS_{1/2}$ series, the contribution from core polarization is less than 2.5%.

We studied the fine-structure splitting of the nD_J series. The fine-structure splitting, Δ_{fs} , can be expanded in terms of a power series in the effective principal quantum number, $[n - \tilde{\delta}^{(l,J=l\pm 1/2)}]$, [53]:

$$\Delta_{\text{fs}} = \sum_{q=1}^{\infty} \frac{\xi_q^{(l)}}{[n - \tilde{\delta}^{(l,J=l\pm 1/2)}(n)]^{2q+1}}. \quad (3)$$

The weighted average quantum defect, $\tilde{\delta}^{(l,J=l\pm 1/2)}(n)$,

TABLE III. Fine-structure interval parameters determined for nD_J series both experimentally (Exp) and numerically (Num). The quoted uncertainties are the standard deviations of the fit.

$nD_{3/2} \rightarrow nD_{5/2}$	$\xi_1^{(l)}$ (kHz)	$\xi_2^{(l)}$ (kHz)	$\xi_3^{(l)}$ (kHz)
Exp [this work]	$6.01624(22) \times 10^{10}$	$-3.38(24) \times 10^{10}$	$8(6) \times 10^{11}$
Exp [53]	$6.02183(60) \times 10^{10}$	$-5.8(8) \times 10^{10}$	0
Num [this work]	6.547×10^{10}	5.5×10^{10}	7.7×10^{11}

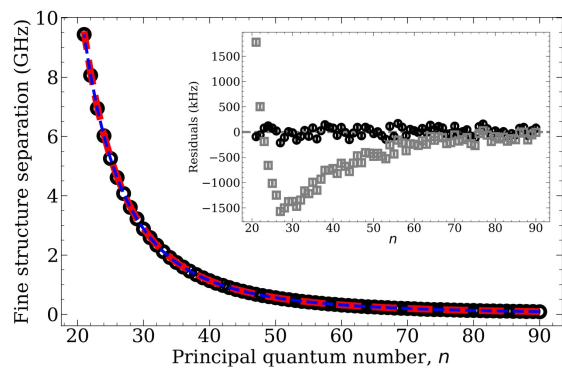


FIG. 3. The fine-structure splitting for nD_J . The red dashed line shows the prediction using Eq. (3). The fitting residuals are given as the black circles in the inset. The fine-structure interval based on the fitting coefficients reported in Ref. [53] is plotted as the blue dashed line for comparison. The corresponding residuals in data in Ref. [53], are shown as gray squares in the inset.

has the form

$$\tilde{\delta}^{(l,J=l\pm 1/2)}(n) = w^{(l,J<l)}\delta^{(l,J<l)}(n) + w^{(l,J>l)}\delta^{(l,J>l)}(n). \quad (4)$$

The weights for the fine-structure splitting, $w^{(l,J)}$, are equal to $1 - \frac{|\langle \mathbf{L} \cdot \mathbf{S} \rangle^{(l,J)}}{\hbar^2(l+1/2)}$, where $\langle \mathbf{L} \cdot \mathbf{S} \rangle^{(l,J)} = \frac{\hbar^2}{2}[J(J+1) - l(l+1) - \frac{3}{4}]$. For the nD_J series, $w^{(2,3/2)} = 0.4$ and $w^{(2,5/2)} = 0.6$.

Using the quantum defect values in Table I and Eq. (4), the measured fine-structure intervals were fit to Eq. (3) to extract $\xi_q^{(l)}$ up to $q = 3$. The values of $\xi_q^{(l)}$ were reported in Ref. [53] based on a single fine-structure interval measurement. The parameters obtained from the measurements presented here are given in Table III. The quality of the fit is evident in Fig. 3; the extracted parameters better describe the fine-structure splittings, Δ_{fs} , at low n . The fitting residuals are randomly distributed around zero as shown in the inset of Fig. 3.

The use of Eq. (3) to describe Δ_{fs} had been proposed and used in previous work [53]. The physical meaning of $\xi_q^{(l)}$, have not been discussed to our knowledge. Here, we justify the expansion (3) by analytically deriving the spin-orbit coupling constant with hydrogenic wave functions, $\langle \frac{1}{r} \frac{dV(r)}{dr} \mathbf{L} \cdot \mathbf{S} \rangle$, for the atomic potential in the form of the sum of the Coulomb and polarization potentials, see Ref. [24]. Moreover, using the effective non-local model potential from Ref. [51] and the precise quantum defects, accurate wave functions and spin-orbit energies for the $nD_{5/2}$ and $nD_{3/2}$ series are determined. The numerical predictions Δ_{fs} are obtained by taking the differences between the expectation values of the spin-orbit coupling operator of the two series [24]. They are fit to Eq. (3) to extract $\xi_q^{(l)}$, as shown in Table III. The difference in the sign of $\xi_2^{(l)}$ may result from the model potential adopted

for the numerical calculations. Importantly, the values of the leading coefficient for both the experimental and numerical approaches, $\xi_1^{(l)}$, are of similar order of magnitude. We note that the weighted average quantum defect, $\tilde{\delta}^{(l, J=l\pm 1/2)}(n)$, should be weighted by the total angular momenta of the $nD_{5/2}$ and $nD_{3/2}$ series, rather than being weighted equally as was done in Ref. [53].

Using our quantum defects and those of Ref. [49] for the P states, we computed reduced electric-dipole matrix elements for $nP_J \leftrightarrow n'D_{J'}$ transitions of Cs. The calculated matrix elements for the low-lying Rydberg states agree within theoretical uncertainties, $< 3\%$, with high-precision, relativistic, all-order many-body calculations of Safronova *et al.* [21], which are computationally sophisticated and resource intensive to perform. With accurate quantum defects, garnered from high n states, accurate wave functions and matrix elements can be obtained for all n , notably for low n where the spectroscopy is difficult to carry-out because of the energy separations between different states. The full comparison table of the matrix elements for the $nP_J \leftrightarrow n'D_{J'}$ transitions is presented in the supplemental material, Table S3 [24].

In summary, we presented high precision, absolute frequency measurements of Cs energy levels from the $|6S_{1/2}, F=3\rangle$ hyperfine ground state to $|nS_{1/2} (n=23-90)\rangle$, $|nD_{3/2} (n=21-90)\rangle$, and $|nD_{5/2} (n=21-90)\rangle$ Rydberg states with an accuracy of < 72 kHz. We investigated the validity of the modified Ritz expansion and conclude that a modified Ritz expansion with only even quantum defect terms can accurately describe the energy levels of the Cs $nS_{1/2}$ and nD_J states. By fitting the absolute-frequency measurements to the modified Ritz formula, Eq. (1), we determine the quantum defects of the Cs $nS_{1/2}$, $nD_{3/2}$, and $nD_{5/2}$ series and the ionization energy. The ionization energy was found to be $31406.46775148(14)$ cm^{-1} . At the current level of precision, we find the quantum defect expansion can be terminated at the third order. We separated the contributions from core polarization and core penetration. For the nD_J series, the contribution from core polarization is about 40%, while for the $nS_{1/2}$ series, the contribution is less than 2.5%. Using improved Cs Rydberg wave functions derived from the quantum defects, we recalculated reduced electric-dipole matrix elements for the $nP_J \leftrightarrow n'D_{J'}$ transitions. The obtained matrix elements are found to be in agreement with high level, many-body relativistic calculations at low n , where our measurements were extrapolated.

Some aspects of prior work that were not accurate have been corrected, such as the form of the fine-structure formula and the number of quantum defect parameters required to describe the spectrum at our level of precision. The accuracy of the wave functions derived from the energy levels of the Cs atom promise to enable a host of important calculations that are not possible to do accurately now, such as those in few-body physics

involving Rydberg states and their interatomic potentials. Furthermore, the accuracy of the dipole moments between different Rydberg states pushes Rydberg-atom-based sensors towards becoming a primary standard for radio frequency fields. The current state of art transition dipole moments for Cs Rydberg RF transitions are accurate to within 0.5 % [54]. Precise knowledge of the atomic wave functions is necessary not only to confirm this assertion but to improve the accuracy. Future work will consist of constructing a new model potential [51] for Cs and the verification of the transition dipole moments.

This work has been supported by The National Research Council Internet of Things: Quantum Sensors Challenge program through Contract No. QSP-058-1. The calculations were supported at ITAMP by a grant from the US National Science Foundation.

* e-mail: jshaffer@qvil.ca

† e-mail: hrs@cfa.harvard.edu

- [1] M. S. Safronova, D. Budker, D. DeMille, D. F. J. Kimball, A. Derevianko, and C. W. Clark, Search for new physics with atoms and molecules, *Rev. Mod. Phys.* **90**, 025008 (2018).
- [2] E. G. Myers, High-precision atomic mass measurements for fundamental constants, *Atoms* **7**, 37 (2019).
- [3] A. D. Cronin, J. Schmiedmayer, and D. E. Pritchard, Optics and interferometry with atoms and molecules, *Rev. Mod. Phys.* **81**, 1051 (2009).
- [4] M. C. Weisskopf, J. P. Carrico, H. Gould, E. Lipworth, and T. S. Stein, Electric dipole moment of the cesium atom. A new upper limit to the electric dipole moment of the electron, *Phys. Rev. Lett.* **21**, 1645 (1968).
- [5] S. A. Murthy, D. Krause, Jr., Z. L. Li, and L. R. Hunter, New limits on the electron electric dipole moment from cesium, *Phys. Rev. Lett.* **63**, 965 (1989).
- [6] W. Bernreuther and M. Suzuki, The electric dipole moment of the electron, *Rev. Mod. Phys.* **63**, 313 (1991).
- [7] C. Chin, V. Leiber, V. Vuletić, A. J. Kerman, and S. Chu, Measurement of an electron's electric dipole moment using Cs atoms trapped in optical lattices, *Phys. Rev. A* **63**, 033401 (2001).
- [8] G. Wilpers, T. Binnewies, C. Degenhardt, U. Sterr, J. Helmcke, and F. Riehle, Optical clock with ultracold neutral atoms, *Phys. Rev. Lett.* **89**, 230801 (2002).
- [9] D. Pan, B. Arora, Y.-m. Yu, B. K. Sahoo, and J. Chen, Optical-lattice-based Cs active clock with a continual superradiant lasing signal, *Phys. Rev. A* **102**, 041101 (2020).
- [10] A. D. Ludlow, M. M. Boyd, J. Ye, E. Peik, and P. O. Schmidt, Optical atomic clocks, *Rev. Mod. Phys.* **87**, 637 (2015).
- [11] A. Sharma, S. Kolkowitz, and M. Saffman, Analysis of a cesium lattice optical clock, (2022), [arXiv:2203.08708](https://arxiv.org/abs/2203.08708) [quant-ph].
- [12] T. Bothwell, C. J. Kennedy, A. Aeppli, D. Kedar, J. M. Robinson, E. Oelker, A. Staron, and J. Ye, Resolving the gravitational redshift across a millimetre-scale atomic sample, *Nature* **602**, 420 (2022).

- [13] T. M. Graham, M. Kwon, B. Grinkemeyer, Z. Marra, X. Jiang, M. T. Lichtman, Y. Sun, M. Ebert, and M. Saffman, Rydberg-mediated entanglement in a two-dimensional neutral atom qubit array, *Phys. Rev. Lett.* **123**, 230501 (2019).
- [14] M. Saffman, T. G. Walker, and K. Mølmer, Quantum information with Rydberg atoms, *Rev. Mod. Phys.* **82**, 2313 (2010).
- [15] D. Bluvstein, S. J. Evered, A. A. Geim, S. H. Li, H. Zhou, T. Manovitz, S. Ebadi, M. Cain, M. Kalinowski, D. Hangleiter, J. P. Bonilla Ataides, N. Maskara, I. Cong, X. Gao, P. Sales Rodriguez, T. Karolyshyn, G. Semeghini, M. J. Gullans, M. Greiner, V. Vuletic, and M. D. Lukin, Logical quantum processor based on reconfigurable atom arrays, *Nature* **626**, 58 (2024).
- [16] L. Henriot, L. Beguin, A. Signoles, T. Lahaye, A. Browaeys, G.-O. Reymond, and C. Jurczak, Quantum computing with neutral atoms, *Quantum* **4**, 327 (2020).
- [17] L. Pause, L. Sturm, M. Mittenbühler, S. Amann, T. Preuschoff, D. Schäffner, M. Schlosser, and G. Birkl, Supercharged two-dimensional tweezer array with more than 1000 atomic qubits, *Optica* **11**, 222 (2024).
- [18] J. A. Sedlacek, A. Schwettmann, H. Kübler, R. Löw, T. Pfau, and J. P. Shaffer, Microwave electrometry with Rydberg atoms in a vapour cell using bright atomic resonances, *Nature Phys.* **8**, 819 (2012).
- [19] H. Fan, S. Kumar, J. Sedlacek, H. Kübler, S. Karimkashi, and J. P. Shaffer, Atom based RF electric field sensing, *J. Phys. B: At. Mol. Opt. Phys.* **48**, 202001 (2015).
- [20] C. T. Fancher, D. R. Scherer, M. C. S. John, and B. L. Schmittberger Marlow, Rydberg atom electric field sensors for communications and sensing, *IEEE Trans. Quantum Eng.* **2**, 1 (2021).
- [21] M. S. Safronova, U. I. Safronova, and C. W. Clark, Magic wavelengths, matrix elements, polarizabilities, and lifetimes of Cs, *Phys. Rev. A* **94**, 012505 (2016).
- [22] J. Dalibard and C. Cohen-Tannoudji, Laser cooling below the Doppler limit by polarization gradients: Simple theoretical models, *J. Opt. Soc. Am. B* **6**, 2023 (1989).
- [23] J. Zhong-Hua, Y. Jin-Peng, Z. Yan-Ting, C. Xue-Fang, X. Lian-Tuan, and J. Suo-Tang, Systematically investigating the polarization gradient cooling in an optical molasses of ultracold cesium atoms, *Chin. Phys. B* **23**, 113702 (2014).
- [24] See Supplemental Material at [url], which includes Refs. [25–39] for additional information about the spectrum fitting methods, uncertainty analysis and a detailed discussion of the theoretical calculations of electric dipole matrix elements..
- [25] P. V. Bevan, Spectroscopic observations: Lithium and caesium, *Proc. R. Soc. A* **86**, 320 (1912).
- [26] H. R. Kratz, The principal series of potassium, rubidium, and cesium in absorption, *Phys. Rev.* **75**, 1844 (1949).
- [27] J. R. McNally, J. P. Molnar, W. J. Hitchcock, and N. F. Oliver, High members of the principal series in caesium, *J. Opt. Soc. Am.* **39**, 57 (1949).
- [28] H. Kleiman, Interferometric measurements of cesium I, *J. Opt. Soc. Am.* **52**, 441 (1962).
- [29] K. Bockasten, Polarization formula for the 2F -series of CsI, *J. Opt. Soc. Am.* **54**, 1065 (1964).
- [30] K. B. S. Eriksson and I. Wenåker, New wavelength measurements in Cs I, *Phys. Scr.* **1**, 21 (1970).
- [31] C.-J. Lorenzen and K. Niemax, New measurements of the $n^2P_{1/2,3/2}$ energy levels of Cs(I), *J. Quant. Spectrosc. Radiat. Transf.* **22**, 247 (1979).
- [32] C.-J. Lorenzen, K.-H. Weber, and K. Niemax, Energies of the $n^2S_{1/2}$ and $n^2D_{3/2,5/2}$ states of Cs, *Opt. Commun.* **33**, 271 (1980).
- [33] C. J. Sansonetti, K. L. Andrew, and J. Verges, Polarization, penetration, and exchange effects in the hydrogen-like nf and ng terms of cesium, *J. Opt. Soc. Am.* **71**, 423 (1981).
- [34] M. S. O’Sullivan and B. P. Stoicheff, Doppler-free two-photon absorption spectrum of cesium, *Can. J. Phys.* **61**, 940 (1983).
- [35] V. Gerginov, A. Derevianko, and C. E. Tanner, Observation of the nuclear magnetic octupole moment of ^{133}Cs , *Phys. Rev. Lett.* **91**, 072501 (2003).
- [36] B. Rahaman, S. C. Wright, and S. Dutta, Observation of quantum interference of optical transition pathways in Doppler-free two-photon spectroscopy and implications for precision measurements, *Phys. Rev. A* **109**, 042820 (2024).
- [37] C. J. Dedman, K. G. H. Baldwin, and M. Colla, Fast switching of magnetic fields in a magneto-optic trap, *Review of Scientific Instruments* **72**, 4055 (2001).
- [38] I. I. Fabrikant, Interaction of Rydberg atoms and thermal electrons with K, Rb and Cs atoms, *J. Phys. B: At. Mol. Opt. Phys.* **19**, 1527 (1986).
- [39] M. Aymar, C. H. Greene, and E. Luc-Koenig, Multichannel Rydberg spectroscopy of complex atoms, *Rev. Mod. Phys.* **68**, 1015 (1996).
- [40] N. Šibalić, J. D. Pritchard, C. S. Adams, and K. J. Weatherill, ARC: An open-source library for calculating properties of alkali Rydberg atoms, *Comput. Phys. Commun.* **220**, 319 (2017).
- [41] D. H. Meyer, Z. A. Castillo, K. C. Cox, and P. D. Kunz, Assessment of Rydberg atoms for wideband electric field sensing, *J. Phys. B: At. Mol. Opt. Phys.* **53**, 034001 (2020).
- [42] J. Bai, S. Bai, X. Han, Y. Jiao, J. Zhao, and S. Jia, Precise measurements of polarizabilities of cesium nS Rydberg states in an ultra-cold atomic ensemble, *New J. Phys.* **22**, 093032 (2020).
- [43] M. Auzinsh, K. Bluss, R. Ferber, F. Gahbauer, A. Jarmola, M. S. Safronova, U. I. Safronova, and M. Tamaniš, Level-crossing spectroscopy of the 7, 9, and $10D_{5/2}$ states of ^{133}Cs and validation of relativistic many-body calculations of the polarizabilities and hyperfine constants, *Phys. Rev. A* **75**, 022502 (2007).
- [44] H. Saßmannshausen, F. Merkt, and J. Deiglmayr, High-resolution spectroscopy of Rydberg states in an ultracold cesium gas, *Phys. Rev. A* **87**, 032519 (2013).
- [45] K.-H. Weber and C. J. Sansonetti, Accurate energies of nS , nP , nD , nF , and nG levels of neutral cesium, *Phys. Rev. A* **35**, 4650 (1987).
- [46] C.-J. Lorenzen and K. Niemax, Precise quantum defects of nS , nP and nD levels in Cs I, *Z. Phys. A* **315**, 127 (1984).
- [47] Standard atomic weights of the elements 2020, available online at <http://ciaaw.org/atomic-weights>.
- [48] D. Steck, Cesium D line data, available online at <http://steck.us/alkalidata> (revision 2.0.1, 2 May 2008).
- [49] J. Deiglmayr, H. Herburger, H. Saßmannshausen, P. Jansen, H. Schmutz, and F. Merkt, Precision measurement of the ionization energy of Cs I, *Phys. Rev. A*

- [93](#), 013424 (2016).
- [50] C.-J. Lorenzen and K. Niemax, Non-monotonic variation of the quantum defect in Cs nD_J term series, [Z. Phys. A](#) **311**, 249 (1983).
 - [51] M. Marinescu, H. R. Sadeghpour, and A. Dalgarno, Dispersion coefficients for alkali-metal dimers, [Phys. Rev. A](#) **49**, 982 (1994).
 - [52] G. W. F. Drake and R. A. Swainson, Quantum defects and the $1/n$ dependence of Rydberg energies: Second-order polarization effects, [Phys. Rev. A](#) **44**, 5448 (1991).
 - [53] P. Goy, J. M. Raimond, G. Vitrant, and S. Haroche, Millimeter-wave spectroscopy in cesium Rydberg states. Quantum defects, fine- and hyperfine-structure measurements, [Phys. Rev. A](#) **26**, 2733 (1982).
 - [54] M. T. Simons, J. A. Gordon, and C. L. Holloway, Simultaneous use of Cs and Rb Rydberg atoms for dipole moment assessment and RF electric field measurements via electromagnetically induced transparency, [J. Appl. Phys.](#) **120**, 123103 (2016).

Supplemental Material:

Ultra precise determination of $\text{Cs}(nS_{1/2})$ and $\text{Cs}(nD_J)$ quantum defects for sensing and computing: Evaluation of core contributions

Pinrui Shen,¹ Donald Booth,¹ Chang Liu,¹ Scott Beattie,² Claude Marceau,² James P. Shaffer,^{1,*}
Mariusz Pawlak,³ and H. R. Sadeghpour^{4,†}

¹*Quantum Valley Ideas Laboratories, 485 Wes Graham Way, Waterloo, Ontario N2L 6R1, Canada*

²*National Research Council Canada, Ottawa, Ontario K1A 0R6, Canada*

³*Faculty of Chemistry, Nicolaus Copernicus University in Toruń, Gagarina 7, 87-100 Toruń, Poland*

⁴*ITAMP, Center for Astrophysics | Harvard & Smithsonian,
60 Garden St., Cambridge, Massachusetts 02138, USA*

(Dated: November 18, 2024)

I. HISTORICAL VALUE OF THE CS IONIZATION ENERGY

Historical measurements of the Cs ionization energy are summarized in Table S1. The improvements in the measurement uncertainty are illustrated in Fig. S1. The precision of the ionization energy has been improved over the past century.

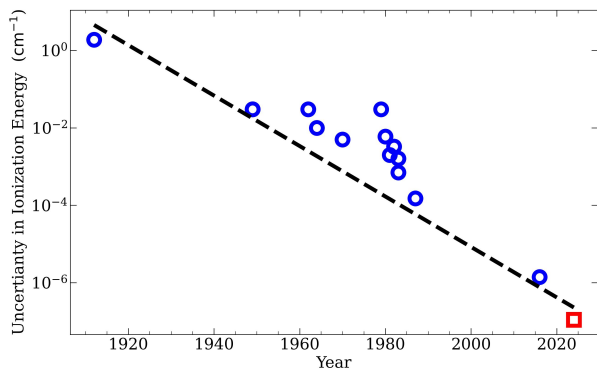


FIG. S1. Improvements in determining the ionization energy of the Cs atom over the last century. The uncertainties are reported in Refs. [1–14]. The red square represents the value reported in this work.

II. ABSOLUTE FREQUENCY FITTING METHOD

Absolute frequency measurements are performed for the $nD_{5/2}$, $nD_{3/2}$, and $nS_{1/2}$ series. For the $nD_{3/2}$ and $nD_{5/2}$ series, the spectrum is fit to a multi-line Gaussian function,

$$f(\nu) = \sum_F (2F + 1) \exp \left[-\frac{(\nu - \nu_F - \nu_0)^2}{2\sigma^2} \right], \quad (1)$$

TABLE S1. The Cs ionization limit in cm^{-1} over the years.

Ref.	year	IE (cm^{-1})
Bevan [1]	1912	31 404.6(1.9)
Kratz [2]	1949	31 406.54(3)
McNally <i>et al.</i> [3]	1949	31 406.32(3)
Kleiman [4]	1962	31 406.450(30)
Bockasten [5]	1964	31 406.432(10)
Eriksson and Wenåker [6]	1970	31 406.454(5)
Lorenzen and Niemax [7]	1979	31 406.46(3)
Lorenzen <i>et al.</i> [8]	1980	31 406.468(6)
Sansonetti <i>et al.</i> [9]	1981	31 406.455 6(20)
Goy <i>et al.</i> [10]	1982	31 406.467 6(33)
O’Sullivan and Stoicheff [11]	1983	31 406.637 6(16)
Lorenzen and Niemax [12]	1983	31 406.471 0(7)
Weber and Sansonetti [13]	1987	31 406.467 66(15)
Deiglmayr <i>et al.</i> [14]	2016	31 406.467 732 5(14)
This work	2024	31 406.467 751 48(14)

which includes all possible hyperfine transitions weighted by the statistical factor of $(2F + 1)$. F represents the total atomic angular momentum. For the $6S_{1/2} \rightarrow nD_{3/2}$ transitions, the possible hyperfine quantum numbers are $F = 2$ and 3. For the $6S_{1/2} \rightarrow nD_{5/2}$ transitions, F can be 1, 2, or 3. σ is the linewidth of the spectral line, assumed to be equal for all of the hyperfine transitions, since the dominant broadening mechanism is Doppler broadening. ν_0 in Eq. (1) is the frequency of the transitions from $|6S_{1/2}, F = 3\rangle$ to the center of gravity of the target Rydberg state, and ν_F is the hyperfine frequency shift from the center of gravity frequency. The value of ν_F can be calculated by [15, 16]

* e-mail: jshaffer@qvil.ca

† e-mail: hrs@cfa.harvard.edu

$$\nu_F = \frac{A_{\text{hfs}}^*(n)}{2}K + B_{\text{hfs}}^*(n)\frac{\frac{3}{2}K(K+1) - 2I(I+1)J(J+1)}{4I(2I-1)J(2J-1)} + C_{\text{hfs}}^*(n)\frac{5K^2(K/4+1) + K[I(I+1) + J(J+1) + 3 - 3I(I+1)J(J+1)] - 5I(I+1)J(J+1)}{I(I-1)(2I-1)J(J-1)(2J-1)}, \quad (2)$$

where

$$K = F(F+1) - I(I+1) - J(J+1). \quad (3)$$

Here, n is the principal quantum number, l is the orbital angular momentum quantum number, J is the total electron angular momentum quantum number, and I is the nuclear spin quantum number. $A_{\text{hfs}}^*(n) = A_{\text{hfs}}/[n - \delta^{(l,J)}]^3$, $B_{\text{hfs}}^*(n) = B_{\text{hfs}}/[n - \delta^{(l,J)}]^3$, and $C_{\text{hfs}}^*(n) = C_{\text{hfs}}/[n - \delta^{(l,J)}]^3$ are the reduced magnetic dipole, the electric quadrupole, and the magnetic octupole hyperfine coupling constants, respectively, where $\delta^{(l,J)}$ is the quantum defect. Rahaman *et al.* [17] performed hyperfine structure measurements for the $7D_J$ states with the quantum interference corrections and reported $A_{\text{hfs}}^*(7) = -1.7110(3)$ MHz, $B_{\text{hfs}}^*(7) = -0.027(7)$ MHz, and $C_{\text{hfs}}^*(7) = -0.02(80)$ kHz for the $7D_{5/2}$ state and $A_{\text{hfs}}^*(7) = 7.3547(8)$ MHz, $B_{\text{hfs}}^*(7) = -0.017(7)$ MHz, and $C_{\text{hfs}}^*(7) = -0.3(4)$ kHz for the $7D_{3/2}$ state. Here, we also analyze the effect of the quantum interference (QI) on the measured Rydberg spectra. In our case, the Rydberg states are detected through ionization and counted by the MCP plate. We use pulse field ionization using a fast risetime pulse applied immediately after optical excitation. The atoms are ionized before any substantial spontaneous decay of the excited Rydberg atoms occurs. To experimentally verify that the effect is minimal in our experiment, we measured the $21D_{5/2}$ spectra at different polarization angles of the second excitation step laser (~ 509 nm) relative to the first excitation step laser (~ 852 nm). The fit of the $21D_{5/2}$ state center frequency is plotted as a function of the polarization angle in Fig. S2. The variation in the frequency of the center of the line shape representing the energy of the Rydberg state, obtained from the fit, is < 20 kHz and is constant within the uncertainty of the experiment. We conclude from the experiment that we can safely ignore the QI effect in our experiment.

For lower n , Eq. (1) is used to extract the center of gravity frequency of the transition. An example of a measured spectrum for $6S_{1/2} \rightarrow 28D_{3/2}$ is shown as Fig. S3(a). As n increases, the hyperfine frequency shift becomes smaller compared to the linewidth. A single Gaussian fitting function is used to extract the center frequency for $n > 60$, where the hyperfine splitting is calculated to be less than 10 kHz. The hyperfine frequency shift is calculated using Eq. (2) and used to correct the center frequency obtained from the Gaussian fit. The uncertainty in the hyperfine constant is also considered and taken as a source of uncertainty. For the $nS_{1/2}$ series, Eq. (1) is reduced to a single Gaussian function without

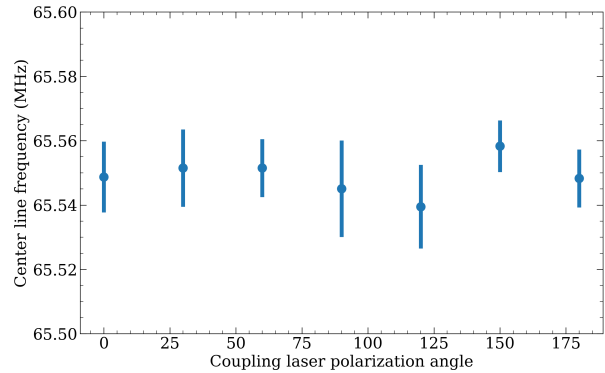


FIG. S2. Spectral line center versus the coupling laser (~ 509 nm) polarization angle relative to the ~ 852 nm laser.

the statistical factor,

$$f(\nu) = \exp\left[-\frac{(\nu - \nu_F - \nu_0)^2}{2\sigma^2}\right], \quad (4)$$

as there is only one possible hyperfine transition, $|6S_{1/2}, F=3\rangle \rightarrow |nS_{1/2}, F'=3\rangle$. The magnetic dipole constant A_{hfs} for the $nS_{1/2}$ series is 13.53(12) GHz [18] and the electric quadrupole constant, B_{hfs} , and the magnetic octupole constant, C_{hfs} , are zero. Similar to the corrections applied for nD_J series, the hyperfine splitting of the $nS_{1/2}$ series is also estimated and corrected. An example of a measured spectrum for $6S_{1/2} \rightarrow 80S_{1/2}$ is shown in Fig. S3(b). The summary of absolute frequency measurements for all three Cs series ($nS_{1/2}$, $nD_{3/2}$, and $nD_{5/2}$) are presented in Table S4.

III. UNCERTAINTY ANALYSIS

In Table S4, the statistical uncertainty is given in the bracket. The dominant source contributing to the statistical uncertainty is the shot-to-shot variation in the Rydberg ion counts. The uncertainty in the number of ions is measured to be $< 10\%$ and contributes less than 10 kHz to the total statistical uncertainty.

The uncertainty caused by the ion count fluctuations increases as the spectral linewidth broadens. Therefore, efforts were made to narrow the spectral linewidth. The dominant source of line broadening is the Doppler effect. To mitigate Doppler broadening, a polarization gradient cooling (PGC) step is used and optimized to cool the atoms to < 10 μ K. With the orthogonal ex-

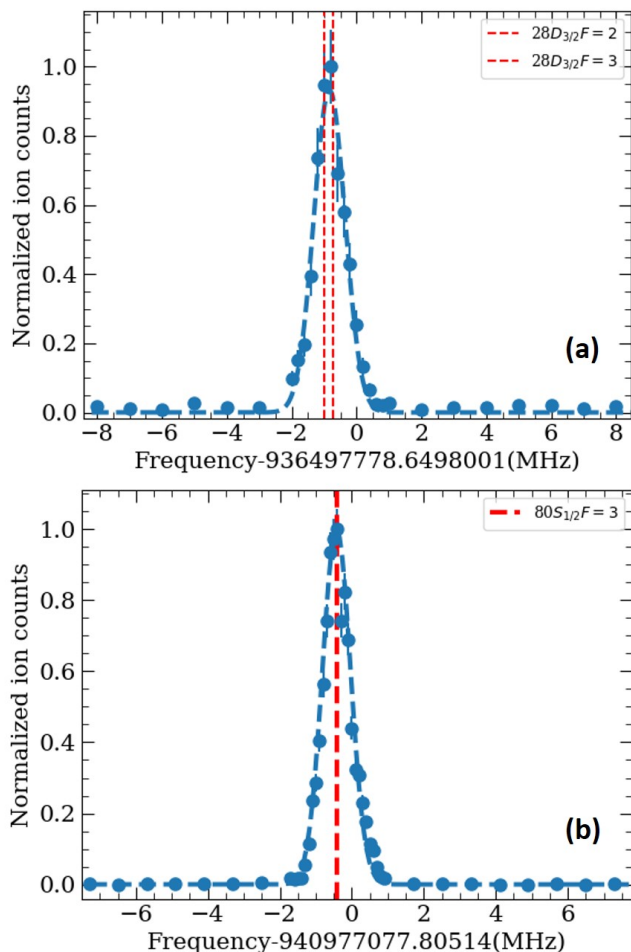


FIG. S3. Panel (a) shows an example of a measured spectrum for $6S_{1/2} \rightarrow 28D_{3/2}$. The spectrum is fit to a multi-line Gaussian function and yields a linewidth of 220 kHz. The corresponding hyperfine transitions are indicated by the red dashed lines. The lineshape is Gaussian because the dominant broadening mechanism is Doppler broadening. Panel (b) shows the spectrum for $6S_{1/2} \rightarrow 80S_{1/2}$, which is fit to a single Gaussian function (see text).

citation laser geometry, the Doppler broadening is estimated to be on the order of 200 kHz, which is close to the linewidth observed in the experiments, ≈ 250 kHz. Other possible contributions to the observed spectral linewidth are radiative decay of the intermediate $6P_{3/2}$ state and power broadening. The radiative decay rate is reduced to < 10 kHz by detuning the first-step laser 90 MHz away from the $6P_{3/2}$ resonance to adiabatically eliminate the intermediate state. The power broadening is suppressed to < 30 kHz by setting both excitation lasers' intensities below their respective saturation intensities. Pressure broadening and transit broadening are estimated to be on the order of 100 Hz, and thus negligible.

An additional contribution to the uncertainty is the determination of the laser frequency. The two excitation lasers are both locked to a GPS steered Rb clock

frequency comb which has a stability of 1.2×10^{-12} for a 10 s averaging time. However, the two lasers pass through AOMs before reaching the atoms. The RF signals driving the AOMs are derived from a quartz oscillator with a stability of 25 ppm. Taking into account the laser locking and the frequency shifts by the AOMs, the uncertainty in the laser frequency is < 2 kHz.

AC Stark shifts induced by the excitation laser fields are another source of uncertainty. Because the experiment was performed after the atoms are released from the molasses, there is no AC Stark shift from the trapping fields. The AC Stark shift induced by the ~ 509 nm laser is calculated to be negligible. Only the AC Stark shift on the ground state, $6S_{1/2}$, induced by the ~ 852 nm laser needs to be considered. To characterize this shift, we measured a series of $54S_{1/2}$ spectra at different first-step laser powers. The measured center frequencies are plotted as a function of the ~ 852 nm laser power, Fig. S4. The slope is found to be (0.45 ± 0.06) kHz/ μ W. For the experiments where we measured the Rydberg state spectra, the power of the ~ 852 nm laser was set to 80.0μ W, which results a (36.0 ± 4.8) kHz blue AC Stark shift. Given that the beam waist and power level of the ~ 852 nm laser are the same for all measurements, the AC Stark shift is applied as a shift for all Rydberg states. The shift has been applied to the values presented in Table S4 to correct the energy levels for a field-free environment. The uncertainty of the AC Stark shift, ± 4.8 kHz, is taken as a contribution to the uncertainty in determining the resonance frequency, listed in Table S2.

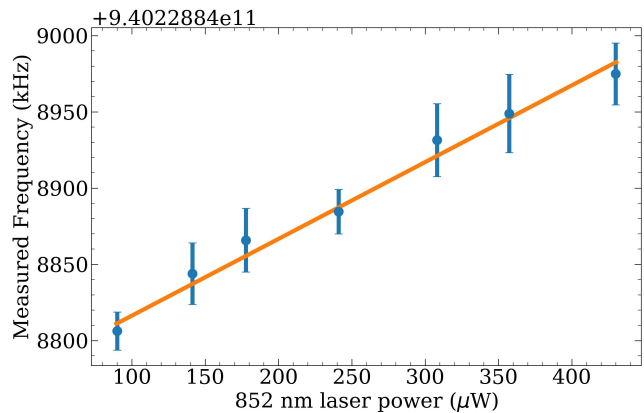


FIG. S4. AC Stark shift measurement. The absolute frequency of the $6S_{1/2} \rightarrow 54S_{1/2}$ transition is measured at different first-step laser power levels. Each data point is an average of five separate measurements and the error bar indicates the uncertainty of each data point derived from the average over the five measurements. The data is fit to a linear function (orange line), yielding a slope of (0.45 ± 0.06) kHz/ μ W.

Stray magnetic fields cause Zeeman shifts of the transitions. Compensation of the background magnetic field is required to obtain accurate spectroscopic measurements. The decay time of the eddy currents in the system as the MOT coils are shutdown is around 12 ms. To increase

TABLE S2. Uncertainties in the determination of the absolute frequency. The amplitude of each uncertainty is listed as the maximum possible value for any states measured in this work.

Sources	Amplitude (kHz)
Ground state AC Stark shift	< 5.0
Zeeman effect shift	< 14.3
DC Stark shift	< 49.0
Hyperfine splitting	< 4.0
Pressure shift	< 2.8
Statistical uncertainty	< 28.0
Total	< 59.0

the decay rate of the eddy currents, we flipped the direction of the current in the MOT coils before extinguishing the magnetic field [19]. Using this approach, the decay time was shortened to less than 2.5 ms. Consequently, a wait time of 3 ms is added between the excitation stage and the extinction of the magnetic fields to reduce the magnetic fields from the eddy current. The other sources of the stray magnetic field are compensated using three pairs of Helmholtz coils placed around the MOT chamber. Microwave (MW) spectroscopy is used to determine the experimental amplitude of the total remaining magnetic field during the atom interrogation period. A similar method was used in Ref. [18] to compensate magnetic fields. The background magnetic field strength is reduced to < 2 mG during the measurement of the Rydberg state transition frequencies, which results in a maximum Zeeman splitting of around 14.3 kHz. The sensitivity to the magnetic field is similar across all Rydberg states because they have the same Landé g -factor. The maximum Zeeman splitting, 14.3 kHz, is treated as a common error for all Rydberg states.

DC Stark effects can cause asymmetric line broadening, as well as a frequency shift. Stray electric fields need to be compensated in order to minimize the DC Stark shift. The stray electric fields are compensated using eight electrodes around the trapped atoms. We use the $160S_{1/2}$ state as a calibration state to minimize the Stark shifts. After carefully adjusting the voltage on each electrode, the electric field is reduced to < 1 mV/cm. For the nD_J series, the DC Stark effect predominately causes broadening of the spectral linewidth. Based on the polarizability of Cs nD_J Rydberg states [20], the DC Stark effect introduces uncertainty that is no greater than 49 kHz for $90D_{5/2}$, while for $n = 27$, the systematic uncertainty induced by the stray electric field is no larger than 30 Hz. For the $nS_{1/2}$ series, the stray electric field primarily induces a frequency shift instead of line broadening. Due to the small polarizability of the Cs $nS_{1/2}$ states [21], the maximum DC Stark effect induced frequency shift is no greater than 1.5 kHz for $90S_{1/2}$.

The pressure shift due to collisions between the Rydberg atoms and the surrounding ground state atoms is

a source of uncertainty. Using the triplet s -wave e^- -Cs scattering length of $-22.7 a_0$ [22] and the peak Cs cloud density of $2 \times 10^{10} \text{ cm}^{-3}$, the maximum pressure shift is estimated to be < 2.8 kHz for $n = 90$.

The main sources of the uncertainties are summarized in Table S2. For the low n states, the hyperfine splitting (< 4.0 kHz) and the Zeeman splitting (< 14.3 kHz) are the key uncertainties, while for the high n states, the DC Stark shift becomes dominant (< 49.0 kHz). The dominant source contributing to the statistical uncertainty is the shot-to-shot variation of the ion counts. The median statistical uncertainty is < 4.0 kHz, and the maximum statistical uncertainty is around 27.4 kHz due to one poor quality measurement.

IV. DISCUSSION OF THE ODD POWER TERMS IN MODIFIED RITZ FORMULA

According to Ref. [23], additional odd power terms should be considered in modified Ritz equation if core polarization makes a significant contribution to the energies, because the odd power terms result from second-order dipole polarization. We fit the nD_J series energy levels to modified Ritz equation with and without the odd power terms and compared the fit parameters. There are no significant changes to the values of the even quantum defects when including the odd power terms in the modified Ritz expansion. The contribution from the odd power terms is less than 0.01%. The quantum defects agree with an estimate of the core-polarization and core-penetration effects in Table II in the main text. We conclude that modified Ritz equation with only even power terms is suitable for accurately describing the energy levels of the Cs $nS_{1/2}$, nP_J , and nD_J states.

V. HIGHER ORDER ($k > 2$) QUANTUM DEFECT PARAMETERS

In this work, we report the quantum defect terms $\delta_{2k,k=0,1,2}$ up to the third order and found the higher order terms ($k > 2$) reported in previous work [12, 13] were negligible within the measurement uncertainties.

Here, we compare our reported quantum defects and prior quantum defects [13] against the observed $nS_{1/2}$ ($n = 8-90$) and $nD_{5/2}$ ($n = 8-90$) energies. The experimental data includes the measurements from Ref. [13] and the measurements in this work. We calculate the deviations characterized by the experimental uncertainty between the data and theoretical calculations using different sets of the quantum defects, as shown in Fig. S5. We find that the prior quantum defects with nonzero $k > 2$ values, obtained by fitting to observed energies for low- n Rydberg levels, do not reproduce our measurements for higher- n levels within uncertainty. However, the quantum defect parameters reported in this work, for high- n levels with zero $k > 2$

terms *reproduce* the previous observed levels at low n , as described in the main text.

It is possible that the lower n states are more sensitive to the higher order terms, but more precise measurements are required to extract their values. Our measurements show that the higher order $k > 2$ terms are not necessary to reproduce all the available data, including the low n states, within the experimental uncertainty for all of the measurements.

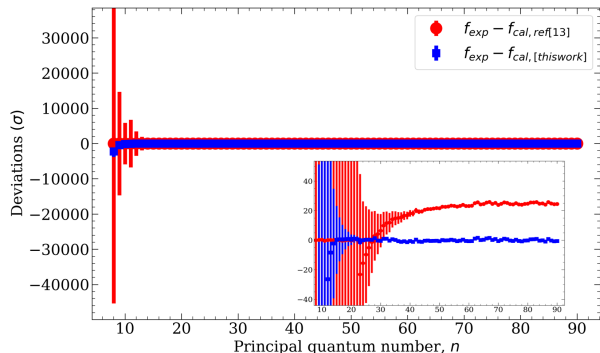


FIG. S5. Deviations between the experimental data and the energy level calculations. The experimental data consist of $nS_{1/2}$ ($n = 8-27$) measurements in Ref. [13] and $nS_{1/2}$ ($n = 28-90$) measurements in this work. Red circles represent the deviations in terms of the experimental uncertainty between the experimental data and the calculated energy levels based on the $nS_{1/2}$ quantum defects in Ref. [13]. Blue squares represent the deviations between the experimental data and the calculated energy levels based on the $nS_{1/2}$ quantum defects in this work. The error bars are the theoretical calculation uncertainties generated from the uncertainties in the quantum defects.

VI. ANALYTICAL FORM OF THE EXPECTATION VALUE OF THE SPIN-ORBIT COUPLING FOR HYDROGENIC WAVE FUNCTIONS

We show that the dominant term of the expectation value of spin-orbit coupling for hydrogenic wave functions scales in proportion to n^{-3} , and the next two as n^{-5} and n^{-7} , assuming the atomic potential to be a Coulomb potential with spherically symmetric core polarization.

The spin-orbit interaction potential is usually given by

$$V^{\text{LS}}(r) = \frac{1}{2\mu^2 c^2} \left(\frac{1}{r} \frac{dV}{dr} \right) \mathbf{L} \cdot \mathbf{S}, \quad (5)$$

where μ is the reduced mass and c is the speed of light. As an attractive potential, we take the Coulomb potential with nuclear charge Ze in conjunction with the core polarization term,

$$V(r) = -\frac{1}{4\pi\epsilon_0} \frac{Ze^2}{r} - \left(\frac{e}{4\pi\epsilon_0} \right)^2 \frac{\alpha_c}{2r^4}, \quad (6)$$

where α_c is static dipole polarizability of the core. The derivative of $V(r)$ divided by r is

$$\frac{1}{r} \frac{dV(r)}{dr} = \frac{Ze^2}{4\pi\epsilon_0} \frac{1}{r^3} + \left(\frac{e}{4\pi\epsilon_0} \right)^2 \frac{2\alpha_c}{r^6}. \quad (7)$$

Acting from both sides with a hydrogenic wave function, we obtain

$$\left\langle \frac{1}{r} \frac{dV}{dr} \right\rangle_{n,l} = \frac{Ze^2}{4\pi\epsilon_0} \left\langle \frac{1}{r^3} \right\rangle_{n,l} + \left(\frac{e}{4\pi\epsilon_0} \right)^2 2\alpha_c \left\langle \frac{1}{r^6} \right\rangle_{n,l}, \quad (8)$$

where

$$\left\langle \frac{1}{r^3} \right\rangle_{n,l} = \frac{Z^3}{a_\mu^3 (l + \frac{1}{2}) l (l + 1) n^3}, \quad (9)$$

$$\left\langle \frac{1}{r^6} \right\rangle_{n,l} = \frac{Z^6}{D} \left(A \frac{1}{n^3} + B \frac{1}{n^5} + C \frac{1}{n^7} \right), \quad (10)$$

$$A = 140, \quad (11)$$

$$B = 20[5 - 6l(l + 1)], \quad (12)$$

$$C = 12l(l^2 - 1)(l + 2), \quad (13)$$

$$D = a_\mu^6 l(l + 1)(2l + 1)[l(l + 1) - 2] \times [4l(l + 1) - 15][4l(l + 1) - 3], \quad (14)$$

and a_μ is the reduced Bohr radius, $a_\mu = \frac{m_e}{\mu} a_0$. Note that Eq. (9) holds for $l > 0$, whereas Eq. (10) for $l > 1$. The effect of the $\mathbf{L} \cdot \mathbf{S}$ term in respect of the l, s, J, m_J quantum numbers is as follows

$$\langle \mathbf{L} \cdot \mathbf{S} \rangle^{(l,J)} = \frac{\hbar^2}{2} \left[J(J + 1) - l(l + 1) - \frac{3}{4} \right]. \quad (15)$$

The fine-structure splitting can be obtained as $\Delta_{\text{fs}} \approx \langle V^{\text{LS}} \rangle_{n,l,J>l} - \langle V^{\text{LS}} \rangle_{n,l,J<l}$, where the dominant terms are proportional to n^{-3} , n^{-5} , and n^{-7} , respectively. This justifies the form of the fine-structure splitting expansion,

$$\Delta_{\text{fs}} = \sum_{q=1}^{\infty} \frac{\xi_q^{(l)}}{[n - \tilde{\delta}^{(l,J=l\pm 1)}(n)]^{2q+1}}. \quad (16)$$

The weighted average quantum defect, $\tilde{\delta}^{(l,J=l\pm 1)}(n) = w^{(l,J<l)} \delta^{(l,J<l)}(n) + w^{(l,J>l)} \delta^{(l,J>l)}(n)$, comprises the quantum defects weighted by the $\mathbf{L} \cdot \mathbf{S}$ term; $w^{(l,J)} = 1 - \frac{|\langle \mathbf{L} \cdot \mathbf{S} \rangle^{(l,J)}|}{\hbar^2(l+1/2)}$.

VII. NUMERICAL CALCULATIONS OF WAVE FUNCTIONS AND REDUCED ELECTRIC-DIPOLE MATRIX ELEMENTS

The Hamiltonian describing the valence electron in the field of an alkali-metal positive-ion core reads (in a.u.)

$$\hat{H} = -\frac{1}{2\mu} \nabla^2 + V_l(r) + V_l^{\text{LS}}(r), \quad (17)$$

where μ is the reduced mass, $V_l(r)$ is the model interaction potential [24], and $V_l^{\text{LS}}(r)$ is the spin-orbit coupling [25]. The l -dependent effective potential, $V_l(r)$, including a polarization term is (in a.u.)

$$V_l(r) = -\frac{1 + (Z-1)\exp[-a_1^{(l)}r]}{r} + \left(a_3^{(l)} + a_4^{(l)}r\right)\exp[-a_2^{(l)}r] - \frac{\alpha_c}{2r^4}\left(1 - \exp\left[-\left(r/r_c^{(l)}\right)^6\right]\right), \quad (18)$$

where Z is the nuclear charge number and α_c is the static dipole polarizability. Five parameters ($r_c^{(l)}$, $a_1^{(l)}$, $a_2^{(l)}$, $a_3^{(l)}$, and $a_4^{(l)}$) are given for different alkali-metal atoms in Ref. [24]. The next term in the Hamiltonian, describing the spin-orbit interaction, could be expressed in the non-trivial form (in a.u.) [25]

$$V_l^{\text{LS}}(r) = \frac{1}{2\mu^2c^2}\left(\frac{1}{r}\frac{dV_l(r)}{dr}\right)\mathbf{L}\cdot\mathbf{S}\left(1 - \frac{1}{2\mu^2c^2}V_l(r)\right)^{-2}. \quad (19)$$

The last part of V_l^{LS} guarantees proper behavior of wave functions at short range.

We calculated the wave functions of the time-independent Schrödinger equation by numerical integration utilizing Numerov's method with energies determined from our quantum defects. We set the integration interval as $[0.01, 2n(n+15)]$ (in a.u.), divided into 4×10^6 equal segments. All obtained functions have attained the appropriate behavior close to the origin as well as asymptotic behavior. We calculated (within composite Simpson's rule) the expectation values of r , V_l^{LS} , and each term of V_l . Subsequently, we estimated the numerical Δ_{fs} for the nD_J series by $\langle V_{l=2}^{\text{LS}} \rangle_{n,l=2,J=5/2} - \langle V_{l=2}^{\text{LS}} \rangle_{n,l=2,J=3/2}$.

The model potential is viewed as a combination interaction of core penetration and core polarization. The first two terms in Eq. (18) are usually considered as the core penetration dominant term, $V_{\text{pen}}(r)$, while the third term is the result of core polarization, $V_{\text{pol}}(r)$. Then, the energy contributions from core polarization and core penetration are $\langle V_{\text{pol}} \rangle$ and $\langle V_{\text{pen}} \rangle$, respectively.

Moreover, based on our results and quantum defects for the nP_J states from Ref. [14], we determined the reduced electric-dipole matrix elements for $n'P_{J'} \leftrightarrow nD_J$ transitions according to

$$\langle J' || r || J \rangle = (-1)^{l'+J+s'+1}\sqrt{(2J'+1)(2J+1)}\delta_{s',s} \times \begin{Bmatrix} l' & J' & s' \\ J & l & 1 \end{Bmatrix} \langle l' || r || l \rangle, \quad (20)$$

where

$$\langle l' || r || l \rangle = (-1)^{l'}\sqrt{(2l'+1)(2l+1)} \times \begin{pmatrix} l' & 1 & l \\ 0 & 0 & 0 \end{pmatrix} \langle n'l'J' || r || nlJ \rangle. \quad (21)$$

The results for low-lying states are compared with the computed values of Safronova *et al.* [26] and for highly excited states with the results from ARC [27], see Table S3.

TABLE S3. The reduced electric-dipole matrix elements (in a.u.).

Transition	Other works	This work
$7D_{3/2} \leftrightarrow 7P_{1/2}$	6.6(2) [26]	6.5814
$7D_{3/2} \leftrightarrow 8P_{1/2}$	32.0(1) [26]	31.9943
$7D_{3/2} \leftrightarrow 9P_{1/2}$	9.0(2) [26]	8.8867
$7D_{3/2} \leftrightarrow 10P_{1/2}$	2.86(8) [26]	2.8524
$7D_{3/2} \leftrightarrow 11P_{1/2}$	1.55(4) [26]	1.5506
$7D_{3/2} \leftrightarrow 12P_{1/2}$	1.03(3) [26]	1.0268
$7D_{3/2} \leftrightarrow 7P_{3/2}$	3.3(1) [26]	3.3328
$7D_{3/2} \leftrightarrow 8P_{3/2}$	14.35(5) [26]	14.3587
$7D_{3/2} \leftrightarrow 9P_{3/2}$	3.56(9) [26]	3.5040
$7D_{3/2} \leftrightarrow 10P_{3/2}$	1.16(4) [26]	1.1603
$7D_{3/2} \leftrightarrow 11P_{3/2}$	0.64(2) [26]	0.6354
$7D_{3/2} \leftrightarrow 12P_{3/2}$	0.42(1) [26]	0.4219
$7D_{5/2} \leftrightarrow 7P_{3/2}$	9.6(3) [26]	9.6960
$7D_{5/2} \leftrightarrow 8P_{3/2}$	43.2(1) [26]	43.2245
$7D_{5/2} \leftrightarrow 9P_{3/2}$	11.1(2) [26]	10.9461
$7D_{5/2} \leftrightarrow 10P_{3/2}$	3.6(1) [26]	3.5939
$7D_{5/2} \leftrightarrow 11P_{3/2}$	1.97(6) [26]	1.9640
$7D_{5/2} \leftrightarrow 12P_{3/2}$	1.31(4) [26]	1.3030
$8D_{3/2} \leftrightarrow 9P_{1/2}$	49.3(1) [26]	49.2834
$8D_{3/2} \leftrightarrow 9P_{3/2}$	22.14(7) [26]	22.1317
$8D_{5/2} \leftrightarrow 9P_{3/2}$	66.6(2) [26]	66.5588
$9D_{3/2} \leftrightarrow 10P_{1/2}$	70.0(1) [26]	69.9676
$9D_{3/2} \leftrightarrow 10P_{3/2}$	31.45(8) [26]	31.4347
$9D_{5/2} \leftrightarrow 10P_{3/2}$	94.5(2) [26]	94.4738
$10D_{3/2} \leftrightarrow 11P_{1/2}$	94.1(2) [26]	94.0566
$10D_{3/2} \leftrightarrow 11P_{3/2}$	42.29(9) [26]	42.2721
$10D_{5/2} \leftrightarrow 11P_{3/2}$	127.0(2) [26]	126.9827
$11D_{3/2} \leftrightarrow 12P_{1/2}$	121.6(2) [26]	121.5538
$11D_{3/2} \leftrightarrow 12P_{3/2}$	54.66(9) [26]	54.6452
$11D_{5/2} \leftrightarrow 12P_{3/2}$	164.1(2) [26]	164.0899
$30D_{3/2} \leftrightarrow 30P_{1/2}$	164.5663 [27]	164.5625
$30D_{3/2} \leftrightarrow 30P_{3/2}$	89.8979 [27]	89.8519
$30D_{5/2} \leftrightarrow 30P_{3/2}$	255.9199 [27]	255.7829
$40D_{3/2} \leftrightarrow 40P_{1/2}$	297.6955 [27]	297.6939
$40D_{3/2} \leftrightarrow 40P_{3/2}$	163.4144 [27]	163.3215
$40D_{5/2} \leftrightarrow 40P_{3/2}$	464.5782 [27]	464.2992
$50D_{3/2} \leftrightarrow 50P_{1/2}$	469.9097 [27]	469.9095
$50D_{3/2} \leftrightarrow 50P_{3/2}$	258.6886 [27]	258.5334
$50D_{5/2} \leftrightarrow 50P_{3/2}$	734.8516 [27]	734.3844
$60D_{3/2} \leftrightarrow 60P_{1/2}$	681.2107 [27]	681.2114
$60D_{3/2} \leftrightarrow 60P_{3/2}$	375.7211 [27]	375.4885
$60D_{5/2} \leftrightarrow 60P_{3/2}$	1066.7426 [27]	1066.0418
$70D_{3/2} \leftrightarrow 70P_{1/2}$	931.5993 [27]	931.6004
$70D_{3/2} \leftrightarrow 70P_{3/2}$	514.5122 [27]	514.1874
$70D_{5/2} \leftrightarrow 70P_{3/2}$	1460.2520 [27]	1459.2724
$80D_{3/2} \leftrightarrow 80P_{1/2}$	1221.0759 [27]	1221.0769
$80D_{3/2} \leftrightarrow 80P_{3/2}$	675.0622 [27]	674.6302
$80D_{5/2} \leftrightarrow 80P_{3/2}$	1915.3803 [27]	1914.0768

TABLE S4. Absolute frequency measurements and the statistical uncertainties of transitions from the $|6S_{1/2}, F = 3\rangle$ hyperfine ground state to the center of gravity of the $nS_{1/2}$, $nD_{5/2}$, $nD_{3/2}$ states. The statistical uncertainties are presented in the brackets.

n	$\nu_{S_{1/2}}$ (kHz)	$\nu_{D_{5/2}}$ (kHz)	$\nu_{D_{3/2}}$ (kHz)
21	—	931969904159.4(6.2)	931960462840.3(16.9)
22	—	932925420315.1(9.9)	932917355120.8(27.0)
23	932386112252.8(10.9)	933744762535.1(6.1)	933737818429.9(5.3)
24	933281572697.2(9.1)	934452628487.4(8.2)	934446607025.4(5.7)
25	934051877594.8(6.0)	935068360508.0(5.3)	935063105302.8(7.6)
26	934719309793.5(6.2)	935607280846.3(4.3)	935602667250.9(11.4)
27	935301404781.5(5.8)	936081653844.5(6.7)	936077581723.7(25.5)
28	935812114821.2(6.6)	936501390829.7(11.6)	936497778401.0(9.4)
29	936262652614.1(6.6)	936874570954.1(11.0)	936871351515.9(14.4)
30	936662113134.8(23.2)	937207833091.9(3.5)	937204951761.9(9.0)
31	937017935503.2(7.8)	937506674118.6(7.4)	937504085293.8(17.5)
32	937336251966.1(6.8)	937775676305.4(12.9)	937773341520.9(27.4)
33	937622154361.1(6.6)	938018683599.5(12.0)	938016570610.9(21.0)
34	937879899105.2(5.8)	938238940313.9(6.9)	938237022105.7(20.4)
35	938113065775.6(5.9)	938439200875.3(7.1)	938437453971.2(10.3)
36	938324682925.2(7.5)	938621813939.2(11.5)	938620218885.2(18.0)
37	938517326596.3(6.1)	938788794105.1(6.1)	938787333466.2(11.6)
38	938693199099.5(13.8)	938941875772.7(8.4)	938940534869.6(13.0)
39	938854192054.4(6.7)	939082559923.6(6.3)	939081326162.6(11.3)
40	939001938005.6(4.9)	939212149979.8(5.3)	939211012223.6(11.8)
41	939137851248.8(5.5)	939331782115.4(3.3)	939330730785.5(6.5)
42	939263162645.1(4.3)	939442451581.3(3.2)	939441477865.5(6.1)
43	939378946543.6(4.4)	939545031475.7(2.8)	939544128149.5(4.5)
44	939486145108.6(5.6)	939640291542.0(3.8)	939639452038.1(4.0)
45	939585586643.1(5.6)	939728912110.0(2.2)	939728130311.4(4.1)
46	939678001804.1(3.9)	939811496008.9(2.3)	939810766742.1(3.9)
47	939764037301.9(4.5)	939888579281.8(4.5)	939887898202.6(4.5)
48	939844267171.4(3.3)	939960639986.8(3.9)	939960602633.6(6.9)
49	939919202219.9(4.1)	940028105046.6(2.7)	940027507933.1(5.2)
50	939989298297.8(3.1)	940091356980.5(2.3)	940090796847.7(6.3)
51	940054963356.3(3.7)	940150739757.1(3.0)	940150213503.5(4.0)
52	940116562993.4(3.2)	940206562229.9(3.3)	940206067286.4(5.1)
53	940174426104.1(3.2)	940259103796.2(3.9)	940258637730.8(4.0)
54	940228848894.2(3.3)	940308616656.9(2.8)	940308176949.6(4.0)
55	940280098714.1(2.8)	940355328595.1(2.5)	940354913714.3(3.4)
56	940328417535.4(2.6)	940399447726.2(2.7)	940399055410.9(4.0)
57	940374024757.6(2.6)	940441161862.7(2.7)	940440790798.0(3.7)
58	940417119508.6(2.8)	940480642898.3(3.0)	940480291683.7(3.7)
59	940457882873.4(2.7)	940518047613.3(2.9)	940517714586.4(4.0)
60	940496480189.1(2.9)	940553518755.5(2.8)	940553202814.9(3.7)
61	940533062211.7(3.9)	940587187563.1(2.9)	940586887573.7(4.0)
62	940567766937.4(2.6)	940619174003.0(2.9)	940618888798.3(4.0)
63	940600720478.7(2.8)	940649588356.1(3.1)	940649317128.1(4.6)
64	940632038624.7(2.5)	940678532080.7(3.3)	940678273721.2(6.8)
65	940661828075.4(2.9)	940706098240.3(3.0)	940705852154.6(3.6)
66	940690186672.2(2.4)	940732373107.7(2.8)	940732138396.3(3.5)
67	940717204520.9(2.7)	940757435910.2(2.9)	940757211965.9(3.4)
68	940742964737.3(2.8)	940781360273.0(3.3)	940781146543.5(4.9)
69	940767544436.6(2.9)	940804213858.0(3.3)	940804009611.6(4.3)
70	940791014390.2(2.6)	940826059993.4(2.9)	940825864543.3(4.0)
71	940813440688.8(2.9)	940846956605.6(3.2)	940846769709.6(5.1)
72	940834884192.3(3.2)	940866958354.9(2.9)	940866779386.3(4.3)
73	940855401394.3(3.0)	940886115318.8(3.1)	940885943816.9(4.5)
74	940875044929.6(3.0)	940904474457.7(3.0)	940904310172.5(3.9)
75	940893863785.4(2.6)	940922079455.2(3.8)	940921921920.8(4.3)
76	940911903524.6(2.5)	940938971360.0(3.5)	940938819935.9(4.9)
77	940929206377.2(3.4)	940955187877.3(3.0)	940955042412.3(4.1)
78	940945812091.5(4.2)	940970764457.6(2.8)	940970624780.2(5.0)
79	940961757637.3(2.8)	940985734322.3(3.1)	940985600177.7(4.7)
80	940977077468.5(3.0)	941000129023.3(2.8)	940999999914.6(5.0)
81	940991803979.2(3.1)	941013977102.4(3.3)	941013852909.6(4.1)
82	941005967315.5(3.3)	941027306402.3(2.8)	941027186804.4(4.4)
83	941019595894.5(3.0)	941040141871.0(3.0)	941040026757.3(4.0)
84	941032716195.4(3.3)	941052508233.8(3.6)	941052397262.3(6.7)
85	941045353362.2(2.8)	941064427739.9(3.8)	941064320777.0(4.3)
86	941057530672.1(4.0)	941075921921.6(2.9)	941075818628.5(3.8)
87	941069270411.2(3.2)	941087010435.1(3.6)	941086910744.6(3.9)
88	941080592943.8(3.0)	941097712195.3(3.0)	941097616114.7(5.5)
89	941091518016.1(3.5)	941108045350.2(4.5)	941107952468.8(6.4)
90	941102064029.3(3.1)	941118026228.4(4.7)	941117936446.0(7.2)

-
- [1] P. V. Bevan, Spectroscopic observations: Lithium and caesium, *Proc. R. Soc. A* **86**, 320 (1912).
- [2] H. R. Kratz, The principal series of potassium, rubidium, and cesium in absorption, *Phys. Rev.* **75**, 1844 (1949).
- [3] J. R. McNally, J. P. Molnar, W. J. Hitchcock, and N. F. Oliver, High members of the principal series in caesium, *J. Opt. Soc. Am.* **39**, 57 (1949).
- [4] H. Kleiman, Interferometric measurements of cesium I, *J. Opt. Soc. Am.* **52**, 441 (1962).
- [5] K. Bockasten, Polarization formula for the 2F -series of CsI, *J. Opt. Soc. Am.* **54**, 1065 (1964).
- [6] K. B. S. Eriksson and I. Wenåker, New wavelength measurements in Cs I, *Phys. Scr.* **1**, 21 (1970).
- [7] C.-J. Lorenzen and K. Niemax, New measurements of the $n^2P_{1/2,3/2}$ energy levels of Cs(I), *J. Quant. Spectrosc. Radiat. Transf.* **22**, 247 (1979).
- [8] C.-J. Lorenzen, K.-H. Weber, and K. Niemax, Energies of the $n^2S_{1/2}$ and $n^2D_{3/2,5/2}$ states of Cs, *Opt. Commun.* **33**, 271 (1980).
- [9] C. J. Sansonetti, K. L. Andrew, and J. Verges, Polarization, penetration, and exchange effects in the hydrogen-like nf and ng terms of cesium, *J. Opt. Soc. Am.* **71**, 423 (1981).
- [10] P. Goy, J. M. Raimond, G. Vitrant, and S. Haroche, Millimeter-wave spectroscopy in cesium Rydberg states. Quantum defects, fine- and hyperfine-structure measurements, *Phys. Rev. A* **26**, 2733 (1982).
- [11] M. S. O'Sullivan and B. P. Stoicheff, Doppler-free two-photon absorption spectrum of cesium, *Can. J. Phys.* **61**, 940 (1983).
- [12] C.-J. Lorenzen and K. Niemax, Non-monotonic variation of the quantum defect in Cs nD_J term series, *Z. Phys. A* **311**, 249 (1983).
- [13] K.-H. Weber and C. J. Sansonetti, Accurate energies of nS , nP , nD , nF , and nG levels of neutral cesium, *Phys. Rev. A* **35**, 4650 (1987).
- [14] J. Deiglmayr, H. Herburger, H. Saßmannshausen, P. Jansen, H. Schmutz, and F. Merkt, Precision measurement of the ionization energy of Cs I, *Phys. Rev. A* **93**, 013424 (2016).
- [15] D. Steck, Cesium D line data, available online at <http://steck.us/alkalidata> (revision 2.0.1, 2 May 2008).
- [16] V. Gerginov, A. Derevianko, and C. E. Tanner, Observation of the nuclear magnetic octupole moment of ^{133}Cs , *Phys. Rev. Lett.* **91**, 072501 (2003).
- [17] B. Rahaman, S. C. Wright, and S. Dutta, Observation of quantum interference of optical transition pathways in Doppler-free two-photon spectroscopy and implications for precision measurements, *Phys. Rev. A* **109**, 042820 (2024).
- [18] H. Saßmannshausen, F. Merkt, and J. Deiglmayr, High-resolution spectroscopy of Rydberg states in an ultracold cesium gas, *Phys. Rev. A* **87**, 032519 (2013).
- [19] C. J. Dedman, K. G. H. Baldwin, and M. Colla, Fast switching of magnetic fields in a magneto-optic trap, *Review of Scientific Instruments* **72**, 4055 (2001).
- [20] M. Auzinsh, K. Bluss, R. Ferber, F. Gahbauer, A. Jarmola, M. S. Safronova, U. I. Safronova, and M. Tamanis, Level-crossing spectroscopy of the 7, 9, and $10D_{5/2}$ states of ^{133}Cs and validation of relativistic many-body calculations of the polarizabilities and hyperfine constants, *Phys. Rev. A* **75**, 022502 (2007).
- [21] J. Bai, S. Bai, X. Han, Y. Jiao, J. Zhao, and S. Jia, Precise measurements of polarizabilities of cesium nS Rydberg states in an ultra-cold atomic ensemble, *New J. Phys.* **22**, 093032 (2020).
- [22] I. I. Fabrikant, Interaction of Rydberg atoms and thermal electrons with K, Rb and Cs atoms, *J. Phys. B: At. Mol. Opt. Phys.* **19**, 1527 (1986).
- [23] G. W. F. Drake and R. A. Swainson, Quantum defects and the $1/n$ dependence of Rydberg energies: Second-order polarization effects, *Phys. Rev. A* **44**, 5448 (1991).
- [24] M. Marinescu, H. R. Sadeghpour, and A. Dalgarno, Dispersion coefficients for alkali-metal dimers, *Phys. Rev. A* **49**, 982 (1994).
- [25] M. Aymar, C. H. Greene, and E. Luc-Koenig, Multichannel Rydberg spectroscopy of complex atoms, *Rev. Mod. Phys.* **68**, 1015 (1996).
- [26] M. S. Safronova, U. I. Safronova, and C. W. Clark, Magic wavelengths, matrix elements, polarizabilities, and lifetimes of Cs, *Phys. Rev. A* **94**, 012505 (2016).
- [27] N. Šibalić, J. D. Pritchard, C. S. Adams, and K. J. Weatherill, ARC: An open-source library for calculating properties of alkali Rydberg atoms, *Comput. Phys. Commun.* **220**, 319 (2017).